Michael Hindemith,[1] Jonas Heidelberger,[2] and Matthias Wangenheim[3]

Investigation of the Influence of Snow Track Density on Tire Tread Block Traction by Experiments and Discrete Element Method Simulation

REFERENCE: Hindemith, M., Heidelberger, J., and Wangenheim, M., **"Investigation of the Influence of Snow Track Density on Tire Tread Block Traction by Experiments and DEM Simulation,"** *Tire Science and Technology*, TSTCA, Vol. 50, No. 4, October–December 2022, pp. 316–336.

ABSTRACT: While in nature, snow properties change from day to day or even minute by minute, one of the great advantages of lab tests is the stability and reproducibility of testing conditions. In our labs at the Institute of Dynamics and Vibration Research, Leibniz Universität Hannover, we currently run three test rigs that are able to conduct tests with tire tread blocks on snow and ice tracks: High-Speed Linear Tester (HiLiTe), Portable Friction Tester (PFT), and Reproducible Tread Block Mechanics in Lab (RepTiL). In the past years, we have run a project on the influence of snow track properties on friction and traction test results with those test rigs. In this article, we will present a first excerpt of the results concentrating on the RepTiL test rig. Because this rig reproduces the movement of rolling tire tread blocks, we executed a test campaign with special samples for the analysis of snow friction mechanics. We evaluated penetration into the snow, maximum longitudinal force level, and longitudinal force gradient. On the other hand, we varied the snow density while preparing our tracks to assess the influence of the snow track density on the friction mechanics. In parallel, we have accompanied our experiments with discrete element method simulations to better visualize and understand the physics behind the interaction between snow and samples. The simulation shows the distribution of induced stress within the snow tracks and resulting movement of snow particles. Hypotheses for the explanation of the friction behavior in the experiments were confirmed. Both tests and simulations showed, with good agreement, a strong influence of snow density and sample geometry.

KEY WORDS: tread block, snow traction, DEM, snow density

1 Introduction

The frictional performance of a tire on snow-covered roads can be influenced by the nature of the tire but also by the properties of the snow. Changing environmental conditions alter the properties of the snow. New snowfall and repeatedly driving over a snow-covered road surface will change the density of the road surface. For this reason, the influence of snow density on the friction behavior of tire tread blocks is analyzed in this article.

[1] Institute of Dynamics and Vibration Research, Leibniz Universität Hannover, An der Universität 1, 30823 Garbsen, Germany. Email: hindemith@ids.uni-hannover.de

[2] Institute of Dynamics and Vibration Research, Leibniz Universität Hannover, An der Universität 1, 30823 Garbsen, Germany. Email: heidelberger@ids.uni-hannover.de

[3] Corresponding author. Institute of Dynamics and Vibration Research, Leibniz Universität Hannover, An der Universität 1, 30823 Garbsen, Germany. Email: wangenheim@ids.uni-hannover.de

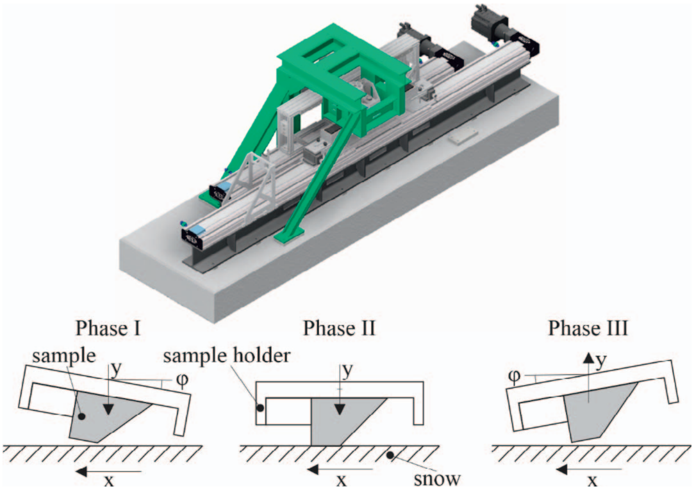

FIG. 1 — *Overview of the test rig Reproducible Tread Block Mechanics in Lab (RepTiL)* [4].

In our lab, artificially produced snow is compressed to a previously defined density and analyzed using CTI hardness [1,2]. The friction investigations are carried out on tread block level at Realistic Pattern in the Lab (RepTiL) [3]. The measurements are performed with Snow Friction Investigation Tool (SFIT) samples, which are made of polytetrafluoroethylene (PTFE). This material allows the analysis of the cohesive friction exclusively, being the dominant mechanism on snow-covered roads [3]. The influence of snow density and different leading-edge angles of the SFIT samples is analyzed and afterward compared with a discrete element method (DEM) simulation.

2 Test Setup

The RepTiL (Fig. 1) is a test rig that allows friction coefficient investigations of tire tread blocks on different track surfaces and ambient conditions. The test rig is built up in a climatic chamber, in which temperatures of –20 to +40 °C can be realized. This allows experiments under summer and winter conditions. The RepTiL offers the possibility to measure the behavior of a single tire tread block replicating the rolling process of a tire in three consecutive phases. Phases I and III describe the roll-in and roll-out of a tire tread block into the footprint. During these phases, the tread sample simultaneously performs a vertical translation $\dot{y}$ and a rotation $\dot{\varphi}$. In phase II, the tire tread block is in contact with the surface while the rotation angle is held constantly at $\varphi = 0°$. In this article, we will solely evaluate phase II; that is, in both the simulation and experiment, we ignore the roll-in and roll-out of the tread block into the contact. The sample can freely penetrate the snow road

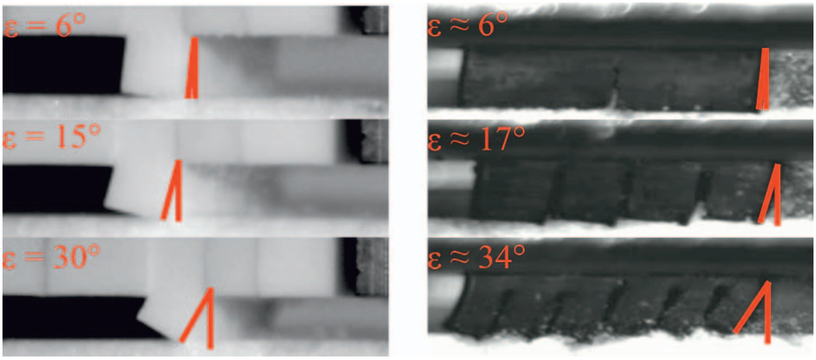

FIG. 2 — *Rigid PTFE SFIT samples with different angles on the leading-edge (left) deflected siped rubber tread block samples (right).*

surface in the *y* direction. A servomotor controls the rotational φ axis. A third controlled degree of freedom is achieved by a horizontal displacement *x* of the track, which is driven by an additional servomotor. This motion determines the slip. Vehicle speed *v* is adjustable between 0 and 1000 mm/s with variable slip ratio. A normal force can be applied up to 1000 N onto the sample holder, which enables us to emulate passenger car contact pressure conditions as well as truck conditions, depending on the contact area of the sample. Piezoelectric force transducers in the sample holder can measure normal force and friction force [4] relative to the sample. In addition, the vertical movement of the sample is recorded during the tests, which is relevant for assessing the sample penetration into soft surfaces such as snow.

2.1 Test Program for Experimental Friction Coefficient Investigations

The friction force of a rubber tread block is generated by these friction mechanisms: cohesion, hysteresis, adhesion, and viscous friction. Cohesion friction, which is the dominant mechanism on snow-covered surfaces, is caused by the tread block milling into the snow surface [3]. To analyze snow cohesion friction, Linke et al. [3] proposed the use of samples made of PTFE, which are called SFIT samples in the following. This material is geometrically rigid and hydrophobic and allows for the exclusive investigation of cohesion friction, as neither adhesion nor hysteresis friction is generated. To mimic the geometric behavior of compliant rubber tread blocks being distorted by tangential snow friction forces, we define different leading-edge angles ε of the SFIT samples (cf. Fig. 2).

The angle of the leading edge of a tread block is determined by the structural stiffness of the tire tread block, affected by the rubber compound stiffness as well as the pattern (i.e., the width and number of sipes per block). Figure 2 shows a comparison between rubber tread samples and SFIT PTFE

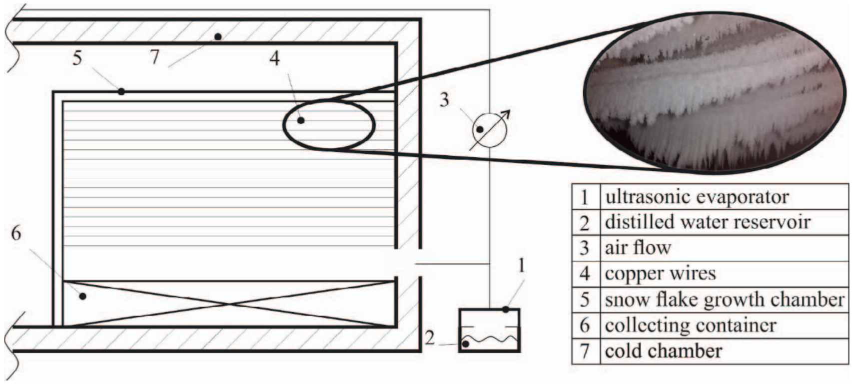

FIG. 3 — *Overview of the basic structure of artificial snow production.*

samples, where it becomes obvious that a harder, wider tread block (as on all-season tires) leads to smaller leading-edge angles than a softer, siped winter tire block. In our tests, the angle ε at the leading edge varies between 6°, 15°, 30°, and 45°. The samples have an identical front clearance angle of $\alpha = 3°$ under the sample. According to [3], the front clearance angle determines the penetration rate of the samples into the snow. Likewise, it was shown in the same article that snow friction is independent from sliding speed.

2.2 Artificially Produced Snow Tracks

The production of artificial snow tracks is carried out in two steps. First, snow is produced in a cold chamber. Then the snow is harvested and pressed into a snow track with a hydraulic press.

The principle for producing artificial snow for the laboratory follows the idea of Schneebeli and Reiweger [5,6]. According to Fig. 3, distilled water is evaporated from a water reservoir with the aid of an ultrasonic evaporator. The water vapor is fed into the growth chamber with clean air flow while maintaining the closed chamber's ambient pressure by pressure compensation. The growth chamber is built in a climate chamber, which has a temperature of –20 °C. At first, the air-vapor mixture is supersaturated; only few condensation nuclei exist. In the growth chamber, copper wires are installed, to which the supersaturated air mixture can contact. These copper wires have a high thermal conductivity. They can remove the sublimation heat, and fast crystallization is stimulated. As a result of the permanently supersaturated air, the water vapor resublimates on the constantly growing ice crystals. Resublimation is possible because the water vapor pressure at the ice crystals is below the ambient pressure and thus below the triple point of water [7].

After the growth period of the snow flakes, the produced snow can be harvested from the snow chamber and pressed into an aluminum frame to form

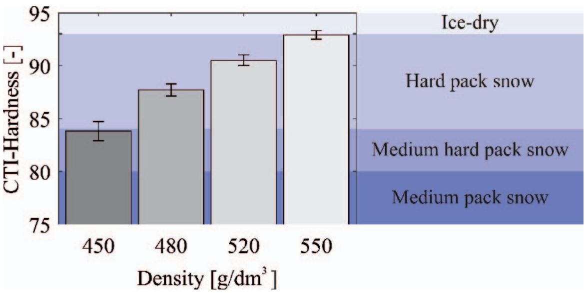

FIG. 4 — *CTI hardness versus snow track density.*

snow tracks. The variation of the snow track density is achieved by pressing different amounts of snow into a constant volume. In our test setup, density (with standard deviation) varies between 450 (0.9), 480 (0.6), 520 (0.5), and 550 (0.4) g/dm^3 (Fig. 4). The hardness of the different snow tracks is determined by a CTI penetrometer [8]. For this purpose, the CTI penetrometer is used to measure defined points on the snow surface. We identified a degressive dependency between the density and the measured CTI hardness. These snow track densities and the associated CTI hardness result in categories of "medium hard pack snow," "hard pack snow," and "ice-dry snowpack" [8]. An increasing snow density is accompanied by an increasing CTI hardness and a decreasing standard deviation: the principle of compressing to a constant volume causes an increasingly homogeneous distribution of the snow mass in the track frame as the snow mass increases.

3 Simulation in DEM

The DEM is a simulation method that was introduced by Cundall and Strack in 1979 [9]. The system to be simulated is discretized into a finite number of particles. The motion of these particles is calculated by solving dynamic equations of motion, taking into account contact laws between the particles. In addition, various mechanical quantities such as stresses, strain rate, and others can be calculated at selected points, which would hardly be possible experimentally. The DEM can therefore be used to investigate the mechanical and rheological behavior of materials, independent of local heterogeneities in the material. The DEM is used by researchers in various fields, such as bulk materials in industry or to simulate fractures in snow layers in nature.

3.1 Modeling of a Snow Track and SFIT Samples

To gain a better understanding of the laboratory measurements of this article, the process is simulated by using DEM. The simulation is performed

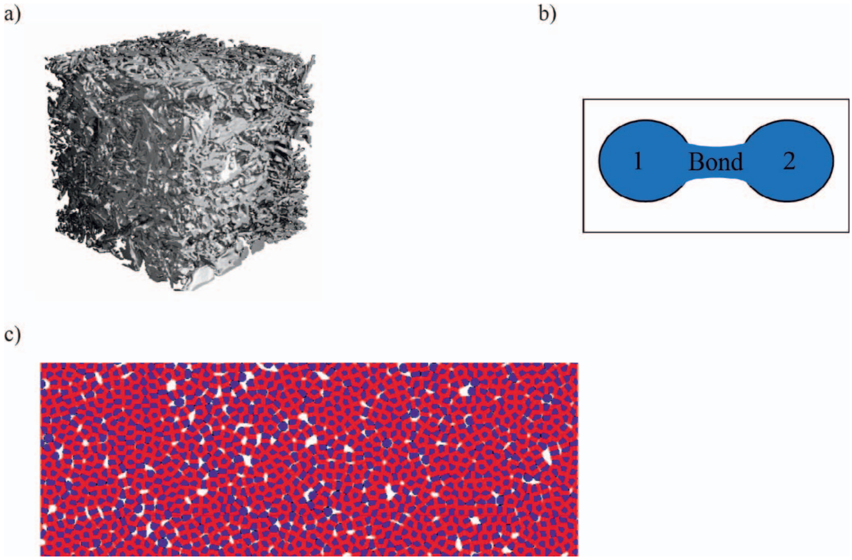

FIG. 5 — *(a) Computer tomography image of a snow cube, [10]. (b) Principle of bound snow particles in PFC. (c) Network of snow particles (blue), bonds (purple), and space (white).*

with the commercial software Particle Flow Code (PFC) by Itasca Consultant GmbH.

For a higher computing efficiency, all simulations are calculated in only two dimensions. The objects of the measurement to be simulated are the snow path and the SFIT samples. The snowpack is represented by a quantity of generated particles. Particles are generated in a way that the space has a defined porosity. The porosity is chosen so that both the network of ice particles and the mass of the snow track are represented. The porosity range of the tracks is between 20% and 30%, representing a density of 550 g/dm^3 down to 450 g/dm^3.

All particles are bonded to neighboring particles during the creation process, when in contact with each other. Figure 5 shows a tomographic image of a snow cube (Fig. 5a), the bonding schematic of two snow particles in the simulation (Fig. 5b), and the resulting network of particles and bonds in (Fig. 5c).

The SFIT sample is represented by a rigid block. A rigid block is a geometry with a defined density. It is nondeformable and follows defined contact laws when coming in contact with particles.

3.2 Contact Law

The contact model used is the parallel bond model according to Potyondy and Cundall [11]. The model was originally developed to describe contacts and fractures in rock mechanics. The model was used by Gaume et al [12] to study

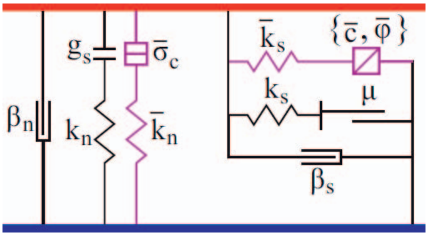

FIG. 6 — *Mechanical model of two bonded particles coming into contact in both the lateral and normal directions. Bonded and unbonded mechanical model, according to PFC documentation.*

the propagation of fractures in snow layers. If two particles come into contact, a distinction is made between unbonded and bonded particles. The contact between two particles is calculated with a linear model in the normal and lateral directions.

If two particles are bonded, there is a connection between them similar to a point of glue. The bond loads are calculated with a normal and a lateral stiffness. The bond can absorb forces and moments with a defined tensile and shear stresses maximum. The normal and lateral direction consists of a spring and damping element in parallel, and the lateral direction has an additional friction element in parallel. The mechanical model is shown in Fig. 6.

The particle contact forces are calculated with the black-colored spring-damper system. The force acting on the bond is calculated by the purple-colored spring system. Two particles come into contact when they approach a defined distance. If the surface gap g_s is equal to or less than zero, the particles are in contact. The following formulae describe the behavior of the mechanical model for the contact of two particles in the two-dimensional case. For a detailed description of the contact law, the contact resolution, and the solution algorithm, please refer to the PFC documentation and to the papers originally published by Cundall and Strack [9] and Potyondy and Cundall [11].

The force displacement law calculates the contact force. The contact force F_c is calculated by

$$F_c = F^l + F^d + \bar{F}. \tag{1}$$

with F^l being the linear force, F^d the dashpot force, and $\bar{F}$ the parallel-bond force. The contact moment consists only of the bending moment on the bond and is given by $M_c = \bar{M}_b$. All three forces are resolved into normal and shear forces by

$$F^l = -F^l_n + F^l_s; F^d = -F^d_n + F^d_s; \bar{F} = \bar{F}_n + \bar{F}_s, \tag{2}$$

with the index n for the normal direction and the index s for the lateral direction. The linear normal force is updated by

$$F_n^l = k_n g_s, g_s < 0 \text{ or } F_n^l = 0, \text{otherwise.} \tag{3}$$

Then the linear shear force is updated. First, a trial shear force $F_s^*$is computed by

$$F_s^* = F_s^l - k_s \Delta\delta_s, \tag{4}$$

with $\delta_{n/s}$ as a relative displacement increment of the normal or shear direction. The shear strength is then calculated by

$$F_s^\mu = \mu F_n^l. \tag{5}$$

The linear shear force F_s^l is updated by

$$F_s^l = F_s^*, F_s^* \leq F_s^\mu$$

or

$$F_s^l = F_s^\mu (F_s^*/F_s^*), \tag{6}$$

otherwise.

The slip status is updated. Slip occurs if $F_s^l = F_s^\mu$ applies. The dashpot force is updated by $F_n^d = F_n^*$ with $F_n^* = 2\beta_n \sqrt{m_c k_n}\, \delta_{\bar{n}}$ and $F_s^d = F_s^*$ with $F_s^* = 2\beta_s \sqrt{m_c k_s}\, \delta_{\bar{s}}$ with $\delta_{n/s}$ being the relative velocity increment in the normal or shear direction. m_c is defined by the types of the two contact partners. $m_c = m_1 m_2/(m_1 + m_2)$ for ball-ball contact and $m_c = m_1$ for a ball-facet contact with $m_{1/2}$, the masses of the contact particles.

Before updating the bond forces, the cross-sectional properties are calculated. First the moment of inertia and the area of the parallel bond cross section are updated by

$$\bar{I} = \frac{2}{3} R^3; \bar{A} = 2\bar{R} \tag{7}$$

with $\bar{R}$ as the minimum radius of the two contact partners. The linear bond force is updated by

$$\bar{F}_n := \bar{F}_n + \bar{k}_n \bar{A} \Delta\delta_n. \tag{8}$$

And the shear bond force is updated by

$$\bar{F}_s = \bar{F}_s - \bar{k}_s \bar{A} \delta_s. \tag{9}$$

The bending moment is updated by

$$\bar{M}_b = \bar{k}_n \bar{I} \Delta\theta_b, \tag{10}$$

with θ_b as the relative bend-rotation increment. The maximum normal and shear stresses at the bond are updated. The normal stress results to

$$\bar{\sigma} = \frac{\bar{F}_n}{\bar{A}} + \frac{\bar{M}_b}{\bar{I}} \bar{R}. \tag{11}$$

If the tensile-strength is exceeded, the bond breaks in tension. In this case, all forces and moments are set to zero. As long as the bond is not broken in tension, the shear strength limit is calculated by

$$\bar{\tau}_c = \bar{c} - \sigma \tan(\bar{\phi}), \tag{12}$$

with the cohesion $\bar{c}$ $\sigma = \frac{\bar{F}_n}{\bar{A}}$ $\sigma = \bar{F}_n / \bar{A}$ as the average normal stress action on the bond and the friction angle $\bar{\phi}$. If the shear strength limit is exceeded, the bond will break in shear. In this case, all forces and moments are set to zero. In the context of this article, the contact law does not yet support rebonding of snow particles in terms of time of pressure.

The contact between rigid blocks and particles is solved by the unbonded contact law. In this case, the parallel-bond forces are zero, and the section of calculating the maximal bond loads are skipped. In addition, adhesional tension forces between the two contact partners cannot be transmitted.

3.3 Simulation Setup

The geometry conforms the real SFIT samples of the laboratory measurements (Fig. 7). A force is applied to the block in a negative Y direction, pressing the block into the snowpack. The block also gains a constant speed in the positive X direction.

The boundary condition of the simulation is a stop condition. The stop condition imposes the constraint that if the body centroid falls outside the model domain, the velocity and spin of the body are zeroed.

Because of two-dimensional modeling, the milled snow is not transported past the sides of the sample as in the real measurements. To simulate the removal of the snow, particles will be deleted if their y position is higher than a defined limit, which is set above the surface of the snowpack. The simulation allows an insight into the load and movement of the individual particles representing the snow in consequence of loads and horizontal movement of the SFIT sample. While moving through the snow, the forces on the sample are logged in normal and horizontal directions. In addition, the position of the sample in the y direction is stored. The translational equations of motion are solved for balls and clumps via the second-order velocity Verlet algorithm [13].

4 Experimental and Simulation Results

In the friction experiments, the SFIT samples were constantly loaded with a normal force $F_{\mathrm{N}} = 130$ N, resulting in a contact pressure of $p = 2.5$ bar. Because the normal force is constant, the evaluation of friction force F_{R} and coefficient of friction μ are equivalent. Vehicle speed V_{x} was set to 100 mm/s. The

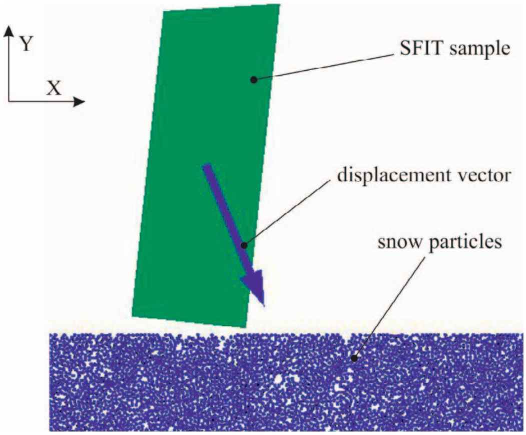

FIG. 7 — *Snow track with SFIT in PFC: the arrow shows the movement direction of the sample for the current time step.*

acceleration slip ratio S of 20% is defined as follows:

$$S = \frac{\omega r - V_x}{V_x} \tag{13}$$

with the tire angular velocity ω and the rolling radius r. Hence, tire circumferential speed and velocity difference result in

$$\omega r = 120 \text{ mm/s and } \Delta v = \omega r - V_x = 20 \text{ mm/s.} \tag{13}$$

The length l of the contact patch for the tire we emulate with our test rig is set to 150 mm, which results in a contact time of

$$t_{\text{cont}} = \frac{l}{\omega r} = 1{:}25 \text{ s.} \tag{13}$$

The sliding distance s holds to

$$s = \frac{\Delta v}{\omega r} l = 25 \text{ mm.} \tag{13}$$

4.1 Variation of Leading-Edge Angle Under Constant Snow Density

Experiments and simulations were first carried out under variation of the leading-edge angle.

Figure 8 shows the penetration depth and friction force for the different SFIT samples on a constant snowpack density of 520 g/dm^3. A negative increase of the penetration depth over the sliding distance (i.e., the penetration gradient) results in a positive increase of the friction force. The increasing snow volume affected by the front of the samples causes the increase in the friction

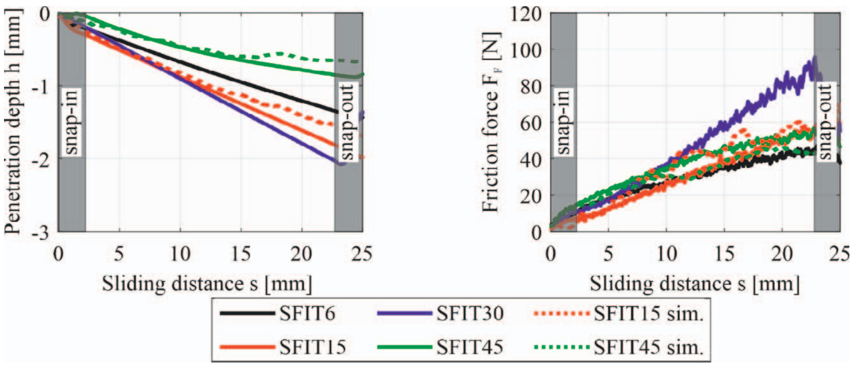

FIG. 8 — *Experimental results: (a) penetration depth and (b) friction force over sliding distance with different sample geometries.*

forces here, except for the SFIT45 sample, which had the greatest leading edge angle of 45°.

The snap-in of the samples is finished after 3-mm sliding distance; the snap-out starts at $s = 22$ mm. Both snap-in and snap-out phases (i.e., combined rotational and vertical motion) are not evaluated in this article. In phase II (compare Fig. 1), the test rig's rotational axis is fixed at 0°. In this phase, the penetration behavior of the samples is approximately linear. With an increase of the leading edge angle from 6° to 30°, the samples penetrate deeper into the snow. This behavior is analogous to the friction force curves (Fig. 8b). An approximately linear increase in the friction force can be seen after the snap-in of the samples. As the leading edge angle increases, a steeper gradient of the friction force can be observed. Only the SFIT45 generates a significantly lower penetration depth with its regressive penetration behavior (i.e., it starts to float). Analogous to this penetration behavior, a degressive increase in friction force can be recognized.

The strong link between penetration depth and friction force curves can be seen in Fig. 8. This influence complicates the analysis of the relation between leading-edge angle and friction force. To characterize the influence of the leading-edge angle, we will evaluate normalized friction force curves versus the penetration.

Simulation and experiment agree well, taking into account that the simulation does not yet consider snow rebonding and growing shear strength. The variation in the friction force evolution can be credited to inhomogeneities in snow distribution.

Figure 9 shows measurement and simulation of the friction force over sample height in the experiment and simulation with varying sample leading-edge angles. The dashed lines indicate a linear approximation of the experimental results.

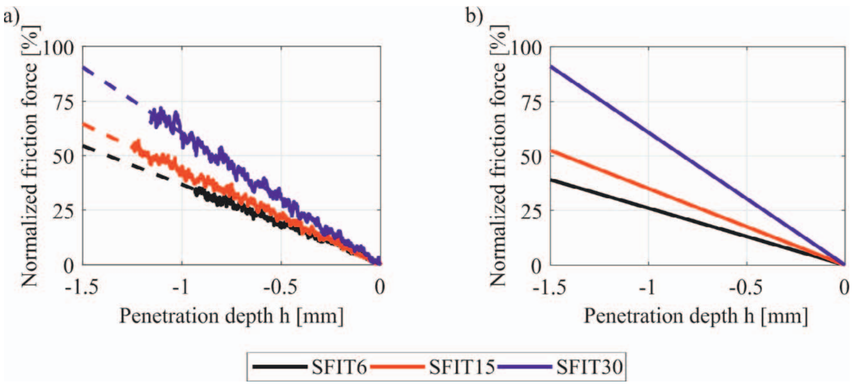

FIG. 9 — *Friction force over penetration depth for different leading-edge angles: (a) experiment; (b) simulation.*

The graphs allows an analysis of the influence of different leading-edge angles at the same penetration depth. The linearly approximated curves show that looking at the same penetration depth, the larger the leading edge angle, the greater the generated friction force for angles between 6° and 30°. Simulation results again show qualitatively fair agreement with experimental results.

4.2 Simulation

To interpret the results, in the first instance we consider the simulation. In the following, the velocity of individual particles is shown in color. Red particles show highest speed; blue particles show no or very slow motion. Figure 10 shows SFIT samples with different leading-edge angles (6° and 30°) while moving through the snow track. The figure shows the samples in a state where they have the same penetration depth.

In Fig. 10, the coloring codes the particle velocity. As the distance traveled increases, the sample penetrates deeper. The contact force breaks the bonds of the particles and sets them into motion in horizontal direction. Not only do the SFIT samples have an effect on the particles in direct contact, but other particles are also exposed to stress, and their connections are destroyed under the influence of the pressure field. The unbonded particles are colored dark green. From a global perspective, the SFIT tread block samples displace the particles and move them forwards-upwards. During the process of moving upwards, the particles generate a resistance force in the X and Y directions. For reasons of numerical effort, particles are deleted by the program when their Y position is greater than a defined limit above the snow surface and they are “flying” freely. With the help of these simulations, we identified three mechanisms contributing to snow cohesion friction by milling:

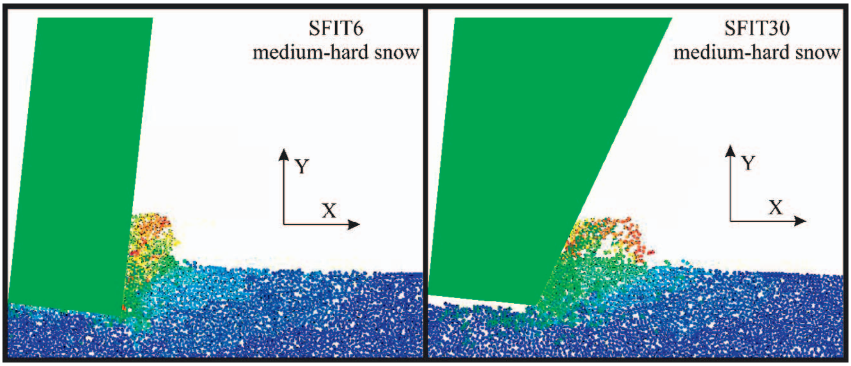

FIG. 10 — *Influence of sample leading-edge angle on snow movement in front of the sample on medium-hard snow.*

4.2.1 Process of Compression. When moving in the X direction, the sample digs deeper into the snow track (cf. Fig. 8a). With higher penetration depth, a proportionally greater share of the normal force is taken up by the front of the samples. This increased force results in a higher pressure field, which sets more particles in motion and compacts them. Figure 11 shows the same sample after different sliding distance.

Compressed snow with a higher density possesses a higher hardness and hence higher shear strength. With increasing the leading-edge angle, the compression process is facilitated by the front surface normal pointing downward compared with the moving direction. The process of moving and compacting snow particles dissipates energy.

4.2.2 Process of Bond Breakage. The simulation shows that a different resultant force F_R appears depending on the leading-edge angle of the SFIT.

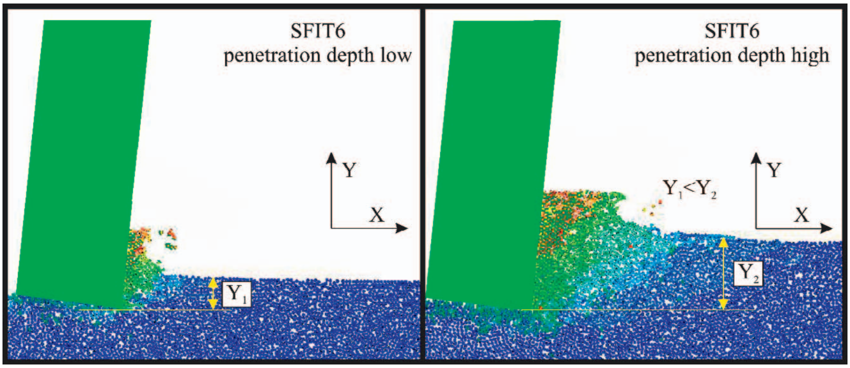

FIG. 11 — *Influence of penetration depth on the movement on medium-hard snow with an SFIT6 sample.*

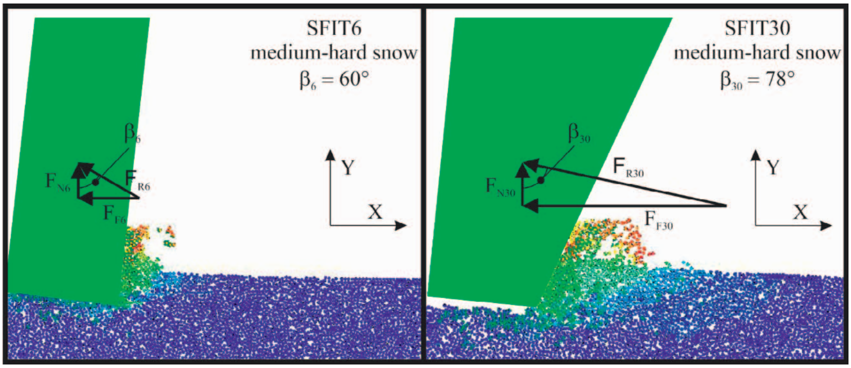

FIG. 12 — *Influence of sample leading-edge angle on resultant force and force angle of attack on medium-hard snow.*

Figure 12 depicts SFIT samples with different leading-edge angles, resultant force, and force triangle under the same constant normal force.

The constant normal force is carried by the contact particles on the front and bottom side. An increasing leading-edge angle leads to an increasing vectorial normal force contribution on the front surface (i.e., the leading edge). In the simulation, the sample bottom side temporarily even loses contact with the snow track. Then the normal force between snow and sample is solely transmitted via the front surface, as can be seen in Fig. 12 for the SFIT30. The friction force results from the breaking of bonds of the snow in front of the sample. By using the simulation data, the direction β of the resultant force vector can be calculated from normal force and friction force. This force angle β rises with an increasing leading-edge angle of the sample as can be seen in Fig. 12.

The experiments show that the force direction (angle β) is not equal to the leading-edge angle ϵ. Comparing different samples, a rising angle β of the resultant force results in higher friction force. This is mainly because of the distribution and size of the stress-induced snow volume increase, while the related shear strength limit of snow grain joints (i.e., particle bonds) remains unaltered.

4.2.3 Process of Snow Removal. To interpret the results discussed in Figs. 8 and 9, experiments and simulations are now taken into consideration. According to the simulation, the load on the sample's front surface increases with increasing leading-edge angle, which also can be seen in an increasing friction force. As an additional result, we can see that the contact area of the front surface ($A_{6;2}$ and $A_{30;2}$, respectively, in Fig. 13) between the samples and the snow becomes larger with the same penetration depth and increasing leading-edge angle.

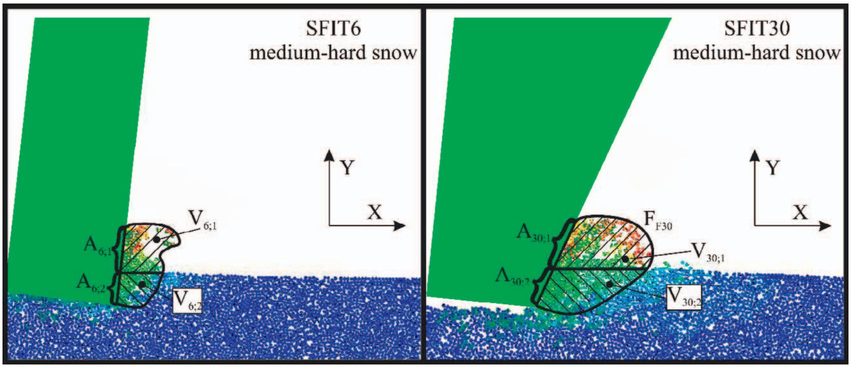

FIG. 13 — *Influence of sample leading-edge angle on resulting friction force and force angle on medium-hard snow.*

The volume of snow, which is set in motion in front of the sample, increases with increasing leading-edge angle, as the comparison of $V_{6;2}$ and $V_{30;2}$ shows in Fig. 13. Energy dissipation arises from friction between the particles. Experiments have shown that this type of snow-snow friction strongly depends on the snow properties, especially on humidity and temperature.

4.3 Variation of Density under Constant Leading-Edge Angle. As a next step, we carried out experiments and simulations under variation of the density of the snow track while keeping the leading-edge angle of the sample constantly at 6°. Figure 14 shows the penetration and friction behavior of the SFIT6 on snow tracks with different densities. The snap-in of the samples is finished after 3-mm sliding distance. After that, the penetration behavior of the samples is approximately linear.

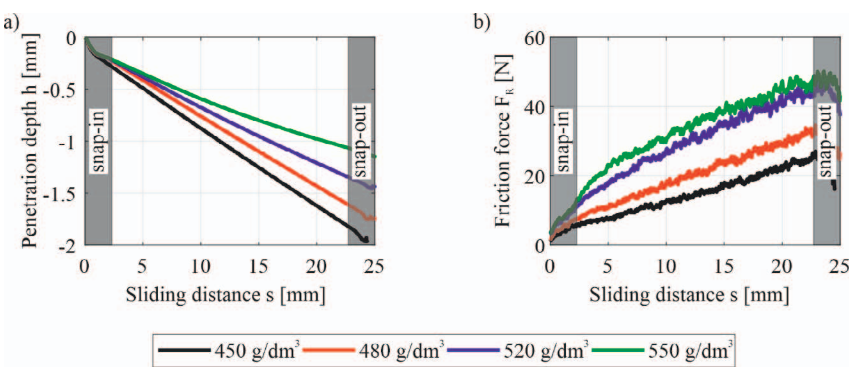

FIG. 14 — *Experimental results with SFIT6: (a) penetration depth and (b) friction force over sliding distance on different snow track densities.*

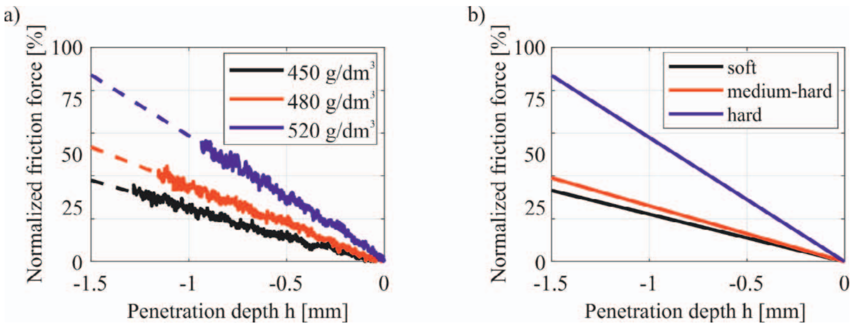

FIG. 15 — *Influence of the snow hardness on friction and penetration with a 6° leading-edge angle: (a) experiment; (b) simulation.*

In coherence with results shown in Figs. 9 and 11, a negative increase of the penetration depth leads to a positive increase of the friction force over sliding distance. The increasing solidified snow volume in front of the samples causes the rise in the friction forces. With an increase of the snow track density, the penetration depth of the samples into the snow is now reduced. At a snow density of 550 g/dm^3, a slightly regressive course of the penetration depth can be observed. Thus, an increase of the snow road density results in a lower penetration depth but in an increasing friction force.

Figure 15 shows a comparison of the friction forces from experiments and qualitative simulation. In the simulation, the density of the snow track was varied by adjusting the porosity of the snow track proportionally to the experimental density variations. A higher porosity leads to a softer snow track, as fewer ice bridges or bonds are formed. The results show higher friction force at the same penetration depth for snow tracks with a higher density and higher hardness, respectively. Experiment and simulation are qualitatively in fair agreement.

In Figure 15b, the SFIT6 is simulated on a soft, a medium-hard, and a hard snow track. At higher snow track hardness, the resultant displacement vector points more upward (compare Fig. 16).

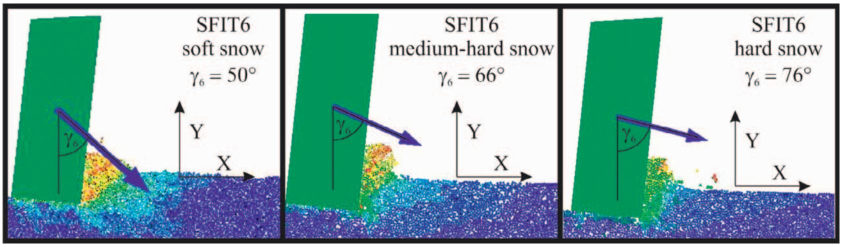

FIG. 16 — *Influence of the snow hardness on snow and sample movement.*

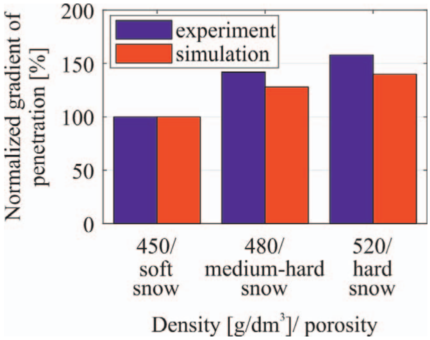

FIG. 17 — *Influence of the snow hardness on snow penetration depth for SFIT6 samples.*

Thus, the sample is penetrating more slowly into the snow track. This is due to the higher resistance of the snow by the increased bonding of the particles. This snow density effect on the penetration behavior of the SFIT samples is shown in Fig. 17 in experiments and simulation (simulations and experimental results deviate approximately 4% for soft snow).

With increasing snow track hardness, the sample penetrates with a flatter gradient into the snow track, indicated by a rise in the vectorial sliding direction γ. Although the friction force is higher, the sample affects fewer particles in the harder snow track at an identical penetration depth. The reason is that the forces applied can be distributed over more and denser bonds. Hence, less bonds are broken (cf. Fig. 18).

Figure 18 shows the particles in motion in front of the SFIT6 sample on snow tracks with different porosity. The volume of snow, which is set in motion in front of the sample, decreases with increasing snow track hardness, as the comparison of $V_{S;2}$, $V_{M;2}$, and $V_{H;2}$ in Fig. 18 shows.

An increase in the snow track density results in an increase in its shear strength limit. The increased strength limit rises the maximum stress until the snow grain connections break. A rise of the angle of attack β of the resultant

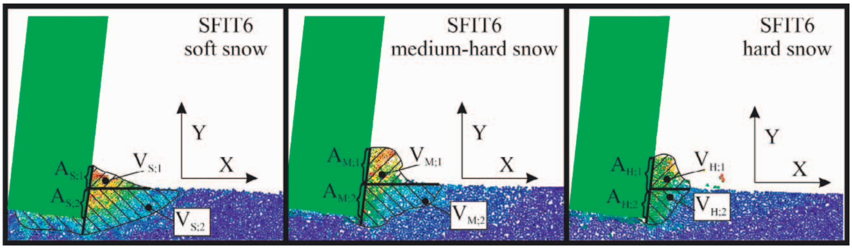

FIG. 18 — *Influence of the snow hardness on the affected snow volume in front of the sample.*

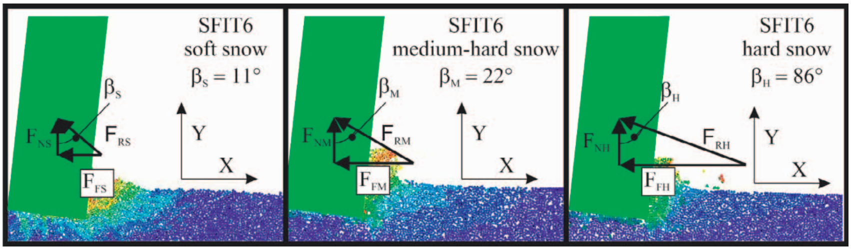

FIG. 19 — *Influence of snow track hardness on resulting friction force and force angle for the SFIT6.*

force in turn causes an increase in the friction force for the SFIT samples according to Fig. 19.

4.4 Variation of Leading-Edge Angle under Variation of Density. To confirm our interpretation of the results, further experiments and simulations were conducted by varying both the leading-edge angle of the sample and the density of the snow track simultaneously. Figure 20 depicts the friction force and the relative gradients of penetration for the variation of snow hardness and SFIT leading-edge angles.

The SFIT6 is set as a reference with 100% gradient of penetration depth (Fig. 20a) and friction force (Fig. 20b) for each snow hardness to analyze the influence of the leading-edge angle.

4.4.1 Gradient of the Penetration. According to Fig. 20a, an increase in the leading-edge angle of the samples from 6° to 30° leads to a steeper gradient of penetration. An increasing snow track density results in a greater spread of the penetration gradient. This result correlates with the observations of the simulations with snow density variations (cf. Fig. 15b).

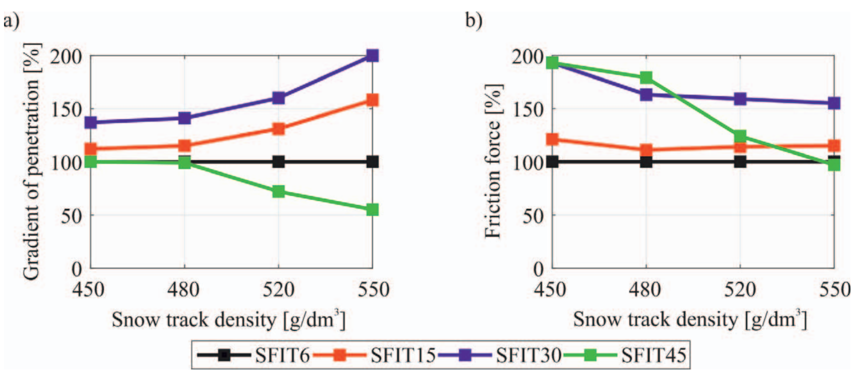

FIG. 20 — *Experimental results of SFIT samples on different snow track densities: (a) gradient of the penetration; (b) friction force.*

The maximum gradient of the penetration of the SFIT30 sample is 200% relative to SFIT6 at a snow track density of 550 g/dm^3. The smallest spread of the measured penetration gradient (137% for SFIT30) is observed at a snow track density 450 g/dm^3.

The SFIT45 test behaves in part contradictory to those findings: from a snow track density of 480 g/dm^3, the SFIT45 generates a continuously decreasing gradient of penetration relative to the SFIT6 sample, because this sample starts to float upward. The minimum of 55% is reached at the hardest snow track with a density of 550 g/dm^3.

4.4.2 Friction Force. The SFIT samples can generate a significantly higher friction force by increasing the leading-edge angle. In our experiments, the SFIT30 sample generates the highest friction of 193% on soft snow and 155% on hard snow, as compared with SFIT6. The SFIT15 sample runs in between SFIT6 and SFIT30 on all snow track densities.

Having an even greater angle at its leading edge, the SFIT45 sample also generates a very high friction force value of 193% and 179% on soft snow, with densities of 450 g/dm^3 and 480 g/dm^3. However, the friction force level drops significantly with increasing snow track density, so that the SFIT45 generates only 97% of the friction the SFIT6 sample shows on hard snow.

These results correlate with the observations of the simulations shown in Fig. 15b. For leading-edge angles from 6° to 30°, a higher friction force can be generated. However, if the leading-edge angle becomes too great, the sample will begin to float on the snow. We were able to observe this behavior with the SFIT45 sample on a snow track with a density of 520 g/dm^3 or higher. In transfer to rubber tires, this means that a high tread block stiffness (determined by material and pattern/block geometry, compare section 2.1) may have higher friction on hard snow than soft compounds with a geometrically compliant pattern.

5 Conclusion

The investigations in this article demonstrate the influence of snow track density on the generated friction force of PTFE tread block samples, referred to here as SFIT (Snow Friction Investigation Tools). The SFIT samples have different leading-edge angles representing rubber tire tread blocks with different compliance defined by their rubber compounds and pattern geometries. PTFE was selected as the material because it shows negligible hysteresis and adhesion friction (i.e., only snow cohesion friction is evaluated in this study).

In the course of this article, a method for the production of reproducible snow tracks with adjustable snow properties is presented. We have accompanied our experiments with DEM simulations to better visualize and understand the physics behind the interaction of snow and tread block samples. While varying

SFIT leading-edge angles in experiment and simulation, we also altered snow track density or porosity, respectively. In addition to the measurement of forces and tread block movement through the snow, the simulation visualizes the snow movement and the breaking of the snow bonds while the SFIT sample is moving into and through the snow track:

- As expected, because of an increase in snow track density, an increase in the friction forces but a decrease of maximal penetration depth can be observed in both simulation and experiments.
- Up to a certain limit, an increase of the leading-edge angle of the tread block causes an increase of the penetration depth and the friction force.
- Above this angle of the leading edge (between 30° and 45°), the tread block sample tends to float on the snow layer, especially on hard snow. The resulting small penetration depth leads to comparably low snow friction.

The leading-edge angle corresponds with the structural stiffness of tire tread blocks: hard blocks found, for example, on all-season tires show small tread block deflection with small leading-edge angles in comparison with soft, siped winter tire tread blocks. Against our expectations, the findings pointed out in this article demonstrate that on hard snow, geometrically stiff tread blocks (e.g., on all-season tires) are able to create significantly more traction than geometrically soft tires (siped winter tires), which may show strong block deflection.

REFERENCES

[1] Ripka, S., Lind, H., Wangenheim, M., Wallaschek, J., Wiese, K., and Wies, B., "Investigation of Friction Mechanisms of Siped Tire Tread Blocks on Snowy and Icy Surfaces," *Tire Science and Technology*, Vol. 40, 2012, pp. 1–24.

[2] Ripka, S., Mihajlovic, S., Wangenheim, M., Wallaschek, J., Wiese, K., and Wies, B., "Tread Block Mechanics on Ice–Snow Surfaces Studied with a New High Speed Linear Friction Test Rig," *VDI BERICHT*, 2086, pp. 239–254.

[3] Linke, T., Wiese, K., Wangenheim, M., Wies, B., and Wallaschek, J., "Investigation of Snow Milling Mechanics to Optimize Winter Tire Traction," *Tire Science and Technology*, Vol. 45, pp. 162–174.

[4] Linke, T., "Untersuchung der Kraftübertragung lamellierter Reifenprofilklötze auf Schneefahrbahnen," Dissertation, Leibniz Universität Hannover, Germany, 2019.

[5] Schleef, S., Jaggi, M., Löwe, H., and Schneebeli, M., "An Improved Machine to Produce Nature-Identical Snow in the Laboratory," *Journal of Glaciology*, Vol. 60, 2014, pp. 94–102.

[6] Enzenhofer, U., Bacher, M., Sokratov, S., Mahr, C., Müller, J., Worthmann, U., and Reiweger, I., "Producing Nature-Like Snow in a Supercold Cloud for Laboratory Experiments," International Snow Science Workshop, Breckenridge, CO, 2016.

[7] Wettlaufer, J. and Furukawa, Y., "Snow and Ice Crystals," *Physics Today*, Vol. 60, 2007, pp. 70–71.

[8] Domeck, D., "Winter Tire Testing as Seen by the Independent Tester," Proceedings of the ISTVS Workshop on Measurement and Evaluation of Tire Performance under Winter Conditions, Alta, UT, 1983, pp. 223–227.

[9] Cundall, P. A. and Strack, D. L., "A Discrete Numerical Model for Granular Assemblies," *Géotechnique*, 1979, Vol. 29, pp. 47–65.

[10] Löwe, H., Spiegel, J. K., and Schneebeli, M., Ordering dynamics of snow under isothermal conditions", WSL, Institute for Snow and Avalanche Research SLF, Davos, Switzerland, 2010.

[11] Potyondy, D. O. and Cundall, P. A., "A Bonded-Particle Model for Rock," *International Journal of Rock Mechanics & Mining Sciences*, Vol. 41, 2004, pp. 1329–1364.

[12] Gaume, J., van Herwijnen, A., Chambon, G., Wever, N., and Schweizer, J., "Snow Fracture in Relation to Slab Avalanche Release: Critical State for the Onset of Crack Propagation," *Cryosphere*, Vol. 11, 2017, pp. 217–228.

[13] Verlet, L., "Computer 'Experiments' on Classical Fluids. I. Thermodynamical Properties of Lennard-Jones Molecules," *Physical Review*, Vol. 159, 1967, pp. 98–103.